Numerical Simulation of Low-Speed Non-Premixed Combustion Using a Preconditioning Technique

V. Bellucci*

CRS4 Research Centre, Cagliari 09123, Italy

C. Bruno†

University of Rome I, Rome 00184, Italy

(Received

A numerical code for the steady-state solution of three-dimensional low-speed flows with combustion is presented. A preconditioned time-marching scheme is applied to the conservative form of the governing equations. The preconditioning matrix multiplies the time-derivatives of the system and circumvents the eigenvalues-caused stiffness at low speed. The formulation is suitable for constant density flows as well as for non-premixed combustion simulated by a presumed pdf model. The $k-\varepsilon$ model accounts for turbulent transport effects. A cell-centered finite volume formulation with a Runge-Kutta time-stepping scheme for the primitive variables is used. The second-order spatial accuracy is achieved by applying to the preconditioned system an Approximate Riemann Solver with MUSCL reconstruction. Numerical techniques as local time-stepping, implicit residual smoothing, and multigrid are used to accelerate the convergence to the steady-state so-

*Research Engineer, Via N. Sauro 10.

†Associate Professor, Dipartimento di Meccanica a Aeronautica, Via Eudossiana 18. Member AIAA.

lution. The convergence behaviour and the validation of the predicted solutions are examined for reacting and non-reacting test cases.

Nomenclature

$\mathbf{A}$	= preconditioned inviscid jacobian
c	= pseudo speed of sound
$\mathbf{F}_E, \mathbf{F}_V$	= inviscid and viscous fluxes
$\mathbf{f}$	= inviscid numerical flux
f	= mixture fraction
f''^2	= mixture fraction variance
$\mathbf{H}$	= source term vector
h	= static entalphy
k	= turbulent kinetic energy
$\mathbf{I}$	= unit tensor
$\mathbf{n}$	= normal to cell interface
Pr, Pr_t	= 0.7, laminar and turbulent Prandtl numbers
p, p_0	= local and average pressure
$\mathbf{Q}$	= primitive variables vector
$\mathbf{R}$	= matrix of inviscid right eigenvectors
Re	= Reynolds number
S	= area of cell interface
t	= time

U = controvariant velocity

$\mathbf{u}$ = velocity vector

$\mathbf{W}$ = conserved variables vector

$\mathbf{\Gamma}$ = preconditioning matrix

β, β_0 = preconditioning parameters

$\Delta(\cdot)$ = $(\cdot)_R - (\cdot)_L$

ε = turbulent dissipation

λ_r = inviscid eigenvalues

μ = $1.8 \cdot 10^{-5}$ kg·m^{-1}·s^{-1}, laminar viscosity

μ_t = turbulent viscosity

ρ = density

ϕ_ℓ = integrated scalar

Ω = cell volume

Subscripts

L, R = left and right interface states

m = faces of the computational cell

Superscripts

T = transpose operator

$\overline{(\cdot)}$ = Reynolds averaging

$\widetilde{(\cdot)}$ = Favre averaging

Introduction

Computational fluid dynamics (CFD) is extensively used to simulate industrially important physical problems in the low Mach number regime where the incompressible condition (i.e. density no longer related to pressure fluctuations) is a valid assumption. Incompressible flows may be both non-reacting flows at low speed (where the density is assumed to be constant) or, as in many combustion applications such as gas turbine combustor chambers flows, where density is assumed to depend only on heat release. [1]

Historically, the numerical simulation of incompressible flows was first investigated using pressure-based approaches. In these methods pressure is updated by a Poisson equation or a correction equation obtained from the continuity equation acting as a constraint condition for the momentum field. [2,3]

On the other hand, time-marching density-based codes have been successfully used (mainly for non reacting flows, but also in combustion) in a wide range of Mach numbers where compressibility is important. These codes have become highly sophisticated in terms of geometry complexity, accurate spatial discretization, and convergence acceleration techniques. Unfortunately, numerical algorithms developed for compressible flows are often ineffective when the Mach number becomes of the order of that found in typical aeroengine combustion chambers [$\sim \mathcal{O}(10^{-3})$] because of the stiffness of the system's eigenvalues. Actually, the time-step of explicit schemes is limited for stability reasons and the maximum allowable time-step is inversely proportional to the largest eigenvalue which, for low speeds, is approximately the speed of sound. However, the time step associated to the waves convected at the fluid speed approaches infinity as the Mach number approaches zero. Hence, the convergence slows dramatically due to the disparity of the wave speeds. Further difficulties are present in constant density flows, where pressure can not be updated by using the equation of state, and also in combustion simulations because of strong density changes due to heat release.

In recent years, preconditioning methods have been used to eliminate the eigenvalues stiffness at low speed. The major advantage of the preconditioning methods is that they may be easily implemented into existing time-marching compressible codes, whose peculiarities are retained. These methods are based on the technique developed by Chorin:[4] an artificial compressibility term under the form of a time-derivative of pressure replaces the time-derivative of density in the continuity equation. Different methods based on the artificial compressibility technique have been suggested. A perturbated form of the governing equations may be obtained by expanding the flow variables in terms of the Mach number. Low-speed flows with volumetric heat addition have been simulated by employing such technique.[5] Alternatively, a suitable preconditioning matrix may be introduced. The preconditioning matrix premultiplies the time-derivatives of the system and rescales the eigenvalues to the same order of magnitude. Preconditioning matrixes have been proposed for incompressible and compressible flows.[6–8] Recently, this preconditioning approach has been proposed to solve reacting and non reacting flows within a wide Mach number range.[9–11]

The objective of this work is to illustrate a preconditionig technique based on the use of a preconditioning matrix and suitable for low-speed flows where the density is constant or depends only on some integrated scalars (i.e. temperature or chemical species' mass fractions). As it will be shown, laminar and turbulent internal flows as well as turbulent diffusion flames modelled by assumed probability density function (pdf) are simulated by such preconditioning technique.

Governing Equations

The continuity, momentum, and $k-\varepsilon$ turbulence model equations are expressed as[12]

$$\frac{\partial \overline{\rho}}{\partial t} + \nabla \cdot (\overline{\rho}\, \tilde{\mathbf{u}}) = 0 \, , \tag{1}$$

$$\frac{\partial \overline{\rho}\, \tilde{\mathbf{u}}}{\partial t} + \nabla \cdot (\overline{\rho}\, \tilde{\mathbf{u}}\, \tilde{\mathbf{u}}) + \nabla P = \nabla \cdot \boldsymbol{\tau} \, , \tag{2}$$

$$\frac{\partial \overline{\rho}\, k}{\partial t} + \nabla \cdot (\overline{\rho}\, k\, \tilde{\mathbf{u}}) = \nabla \cdot \left[\left(\mu + \frac{\mu_t}{\sigma_k} \right) \nabla k \right] + \mathcal{P} - \overline{\rho}\, \varepsilon \, , \tag{3}$$

$$\frac{\partial \overline{\rho}\, \varepsilon}{\partial t} + \nabla \cdot (\overline{\rho}\, \varepsilon\, \tilde{\mathbf{u}}) = \nabla \cdot \left[\left(\mu + \frac{\mu_t}{\sigma_\varepsilon} \right) \nabla \varepsilon \right] + \frac{\varepsilon}{k} \left(c_1\, \mathcal{P} - c_2\, \overline{\rho}\, \varepsilon \right) \tag{4}$$

where $\sigma_k = 1$, $\sigma_\varepsilon = 1.3$, $c_1 = 1.45$, $c_2 = 1.92$ ("standard" $k-\varepsilon$ model),

$$P = \overline{p} + \frac{2}{3}\, \overline{\rho}\, k \, , \tag{5}$$

$$\boldsymbol{\tau} = (\mu + \mu_t) \left(\nabla \tilde{\mathbf{u}} + \nabla \tilde{\mathbf{u}}^T \right) - \frac{2}{3} (\mu + \mu_t) (\nabla \cdot \tilde{\mathbf{u}}) \, , \tag{6}$$

$$\mathcal{P} = \mu_t \left(\nabla \tilde{\mathbf{u}} + \nabla \tilde{\mathbf{u}}^T \right) : \nabla \tilde{\mathbf{u}} - \frac{2}{3} (\nabla \cdot \tilde{\mathbf{u}}) \left[\mu_t (\nabla \cdot \tilde{\mathbf{u}}) + \overline{\rho}\, k \right] \tag{7}$$

Furthermore $\mu_t = c_\mu \, \overline{\rho} \, k^2/\varepsilon$ and $c_\mu = 0.09$.

Non-Reacting Flows

Under the assumption of low speed, the energy equation is given by[1]

$$\frac{\partial \, \overline{\rho} \, \widetilde{h}}{\partial t} + \nabla \cdot \left(\overline{\rho} \, \widetilde{h} \, \tilde{\mathbf{u}} \right) = \nabla \cdot \left[\left(\frac{\mu}{Pr} + \frac{\mu_t}{Pr_t} \right) \nabla \, \widetilde{h} \right] \, . \tag{8}$$

The ideal gas equation of state is expressed as

$$\overline{\rho} = \frac{\gamma}{\gamma - 1} \frac{p_0}{\widetilde{h}} \tag{9}$$

where $\gamma = 1.4$. Eqs. (8) and (9) lead to a constant density flow if the static enthalpy is constant on the inflow and the solid walls are adiabatic.

Non-Premixed Turbulent Combustion Model

Following the conserved scalar approach,[13] a diffusion flame may be simulated by Eqs. (1)-(4) together with equations

$$\frac{\partial \, \overline{\rho} \, \widetilde{f}}{\partial t} + \nabla \cdot \left(\overline{\rho} \, \widetilde{f} \, \tilde{\mathbf{u}} \right) = \nabla \cdot \left[\left(\frac{\mu}{Pr} + \frac{\mu_t}{Pr_t} \right) \nabla \, \widetilde{f} \right] \, , \tag{10}$$

$$\frac{\partial \, \overline{\rho} \, \widetilde{f''^2}}{\partial t} + \nabla \cdot \left(\overline{\rho} \, \widetilde{f''^2} \, \tilde{\mathbf{u}} \right) = \nabla \cdot \left[\left(\frac{\mu}{Pr} + \frac{\mu_t}{Pr_t} \right) \nabla \, \widetilde{f''^2} \right] + 2 \, \frac{\mu_t}{Pr_t} \nabla \, \widetilde{f} \cdot \nabla \, \widetilde{f} - c_f \, \overline{\rho} \, \frac{\varepsilon}{k} \, \widetilde{f''^2} \tag{11}$$

where $c_f = 1$. The assumptions that lead to the conserved scalar model are: two-feed flow (and uniform composition and temperature in the two feeds); low Mach number; Dufour and Soret effects neglected; constant species specific heats; equal diffusion coefficient for all the species; Lewis number equal to one; adiabatic walls;

body forces and radiative flux neglected. The conserved scalar f represents either the normalized non-averaged enthalpy $(h - h_2)/(h_1 - h_2)$ or the mixture fraction (e.g. the mass fraction of material in the mixture originated in feed 1, with $(1 - f)$ originated in feed 2).[13] The variance $\widetilde{f''^2}$ accounts for the fluctuations of $\widetilde{f}$ due to turbulence. The density is assumed to be a function of f alone, implying thermochemical equilibrium, and at low Mach, when the combustor pressure is nearly equal to p_0,

$$\rho = \frac{p_0}{\mathcal{F}(f)} \tag{12}$$

where the function $\mathcal{F}(f)$ (depending on the equilibrium chemistry between a specific fuel and air) is approximated by the N-polynomial fit

$$\mathcal{F}(f) = \sum_{n=0}^{N} c_n f^n \tag{13}$$

obtained by minimizing the Gibb's free energy of the products mixture.[14] The mean density is evaluated by

$$\overline{\rho} = \left[\int_0^1 \frac{\widetilde{P}(f)}{\rho(f)} df\right]^{-1} = p_0 \left[\int_0^1 \mathcal{F}(f)\,\widetilde{P}(f) df\right]^{-1} \tag{14}$$

where $\widetilde{P}(f)$ is the Favre probability density function. Using the assumed β-pdf model,[15] the $\widetilde{P}(f)$ is given by

$$\widetilde{P}(f) = \frac{f^{a-1}(1 - f^{b-1})}{\displaystyle\int_0^1 f^{a-1}(1 - f^{b-1})\,df} \tag{15}$$

where

$$a = \frac{\widetilde{f}^2(1 - \widetilde{f})}{\widetilde{f''^2}} - \widetilde{f}, \qquad b = \frac{\widetilde{f}(1 - \widetilde{f})^2}{\widetilde{f''^2}} - (1 - \widetilde{f}). \tag{16}$$

By substituting Eqs. (13) and (15) in Eq. (14) one has

$$\overline{\rho} = \frac{p_0 \, A_0}{\sum\limits_{n=0}^{N} c_n \, A_n} \tag{17}$$

where the integrals A_n are expressed as[16]

$$\begin{aligned} A_n &= \int_0^1 f^{\,a-1+n} \, (1 - f^{\,b-1}) \, df \\ &= A_0 \prod_{m=1}^{n} \frac{a-1+m}{a+b-1+m} \, . \end{aligned} \tag{18}$$

Preconditioning Method

Following the cell-centered Finite Volume approach, the system of governing equations (1)-(4) plus Eq. (8) or Eq. (10)-(11) can be written in compact form as

$$\frac{d\mathbf{W}}{dt} = -\frac{1}{\Omega} \sum_m \left[(\mathbf{F}_E - \mathbf{F}_V) \cdot \mathbf{n} \right]_m \, S_m + \mathbf{H} \tag{19}$$

where $\mathbf{W} = \left[\overline{\rho} \, , \, \overline{\rho} \, \tilde{\mathbf{u}} \, , \, \overline{\rho} \, \widetilde{\phi_\ell} \right]^T$ with $\widetilde{\phi_\ell} = (k \, , \, \varepsilon \, , \, \tilde{h})$ or $\widetilde{\phi_\ell} = (k \, , \, \varepsilon \, , \, \tilde{f} \, , \, \widetilde{f''^2})$ for non-reacting or reacting flows, respectively.

As noted, time-marching algorithms applied to Eqs. (19) become ineffective at low speed because of the eigenvalues stiffness. Furthermore, in Eqs. (19) the pressure cannot be numerically updated by the equation of state Eq. (9) or Eq. (17). These problems are circumvented by using the following preconditioning technique. By introducing the matrix

$$\mathbf{K} = \begin{bmatrix} 1 & 0 & 0 \\ -\tilde{\mathbf{u}} & \mathbf{I} & 0 \\ -\widetilde{\phi_\ell} & 0 & \mathbf{I} \end{bmatrix} , \tag{20}$$

Eqs. (19) are transformed in the non-conservative form

$$\left(\mathbf{K}\frac{\partial \mathbf{W}}{\partial \mathbf{Q}}\right) \frac{d\mathbf{Q}}{dt} = -\frac{1}{\Omega}\mathbf{K} \sum_m \left[(\mathbf{F}_E - \mathbf{F}_V)\cdot \mathbf{n}\right]_m \; S_m + \mathbf{K}\,\mathbf{H} \tag{21}$$

in terms of $\mathbf{Q} = \left[(P-p_0)\,,\, \tilde{\mathbf{u}}\,,\, \widetilde{\phi_\ell}\right]^T$. The integrated variable $(P-p_0)$ eliminates the roundoff error arising in the computation of pressure and pressure gradients. In the matrix

$$\mathbf{K}\frac{\partial \mathbf{W}}{\partial \mathbf{Q}} = \begin{bmatrix} 0 & 0 & \overline{\rho}_{\widetilde{\phi_\ell}} \\ 0 & \overline{\rho}\,\mathbf{I} & 0 \\ 0 & 0 & \overline{\rho}\,\mathbf{I} \end{bmatrix} \tag{22}$$

the term $(1,1)$ that multiplies the time-derivative of pressure controls the pressure wave speeds and is responsible for the eigenvalues' stiffness. The stiffness is avoided by replacing the matrix (22) with the matrix[6]

$$\mathbf{P}^{-1} = \begin{bmatrix} \dfrac{1}{\beta} & 0 & 0 \\ 0 & \overline{\rho}\,\mathbf{I} & 0 \\ 0 & 0 & \overline{\rho}\,\mathbf{I} \end{bmatrix} \tag{23}$$

where β represents the pressure wave speed of the preconditioned system. Therefore, Eqs. (21) are replaced by

$$\frac{d\mathbf{Q}}{dt} = -\frac{1}{\Omega}\mathbf{\Gamma} \sum_m \left[(\mathbf{F}_E - \mathbf{F}_V)\cdot \mathbf{n}\right]_m \; S_m + \mathbf{\Gamma}\,\mathbf{H} \tag{24}$$

where

$$\mathbf{\Gamma} = \mathbf{P}\,\mathbf{K} = \begin{bmatrix} \beta & 0 & 0 \\ -\dfrac{\tilde{\mathbf{u}}}{\overline{\rho}} & \dfrac{\mathbf{I}}{\overline{\rho}} & 0 \\ -\dfrac{\widetilde{\phi_\ell}}{\overline{\rho}} & 0 & \dfrac{\mathbf{I}}{\overline{\rho}} \end{bmatrix}. \tag{25}$$

In Eqs. (24) pressure is updated by its time-derivative and the equation of state is employed to obtain the density.

By defining $\mathrm{f} = \mathbf{F}_E \cdot \mathbf{n}$, the eigenvalues of $\mathbf{A} = \mathbf{\Gamma}\partial \mathrm{f}/\partial \mathbf{Q}$ are

$$\lambda_r(\mathbf{A}) = U\,,\, U\,,\, U\,,\, U/2 + c,\, U/2 - c \tag{26}$$

where $U = \tilde{\mathrm{u}} \cdot \mathbf{n}$ and $c = \sqrt{(U/2)^2 + \beta}$. In this work β is given by

$$\beta = \beta_0\, U_\infty^2 \tag{27}$$

where U_∞ is a free-stream velocity and β_0 is a constant greater than zero in order to ensure that one eigenvalue is negative for subsonic flows. The value of β is critical for the convergence properties of the method. Actually, well-conditioned λ_r are obtained when β makes the pseudo acoustic wave speed of the same order of the particle velocity (i.e. $\beta_0 = 1$). Nevertheless, when the Reynolds number decreases, the characteristic time of viscosity spreading also decreases, and if β is too small the boundary layer cannot adapt to the too-slowly developing pressure field and fluctuations of separation regions may destroy the convergence.[7] Numerical experiments reported later will illustrate the influence of β on the properties of the numerical scheme.

Solution Procedure

The Roe's Approximate Riemann Solver[17] is used for the spatial discretization of inviscid fluxes. At the interface $(i + 1/2)$ between the adjacent cells $(i\,,\, j\,,\, k\,)$

and $(i+1\,,\,j\,,\,k)$, $\mathbf{f}_{i+1/2}$ is evaluated by using the expression

$$\mathbf{f}_{i+1/2} = \frac{\mathbf{f}_L + \mathbf{f}_R}{2} - \frac{1}{2}\,\mathbf{\Gamma}^{-1}\,|\mathbf{A}_{\,i+1/2}|\,\Delta\mathbf{Q} \tag{28}$$

where states $\mathbf{Q}_L$ and $\mathbf{Q}_R$ are computed by employing the MUSCL approach:[18]

$$\mathbf{Q}_R = \mathbf{Q}_{\,i+1} - \frac{1}{2}\overline{\overline{\Delta\,\mathbf{Q}}}_{\,i+3/2}\,, \tag{29}$$

$$\mathbf{Q}_L = \mathbf{Q}_{\,i} + \frac{1}{2}\overline{\overline{\Delta\,\mathbf{Q}}}_{\,i-1/2}\,. \tag{30}$$

Spurious oscillations are eliminated using

$$\overline{\overline{\Delta\,\mathbf{Q}}}_{\,i+1/2} = \text{minmod}\,\left[\,\mathbf{Q}_{\,i+1} - \mathbf{Q}_{\,i}\,,\,\omega\,\left(\mathbf{Q}_{\,i} - \mathbf{Q}_{\,i-1}\right)\right]\,, \tag{31}$$

$$\text{minmod}\,(x\,,\,y) = \text{sgn}\,(x)\cdot\max\,\{0\,,\,\min\,[|x|\,,\,y\ \text{sgn}\,(x)]\}\ .$$

The value $\omega = 1$ (second-order full-upwind scheme) is employed for all the equations apart from the $k-\varepsilon$ Eqs. (3) and (4), for which $\omega = 0$ (first-order upwind scheme). In Eqs. (28) $|\mathbf{A}| = \mathbf{R}\,|\mathbf{\Lambda}|\,\mathbf{R}^{-1}$ where $|\mathbf{\Lambda}| = \text{diag}\,(|\lambda_r|)$ and arithmetic averaging between $\mathbf{Q}_R$ and $\mathbf{Q}_L$ is used to define the interface values. After rearranging terms, one has

$$|\mathbf{A}|\,\Delta\,\mathbf{Q} = \begin{bmatrix} \beta\,\left[\dfrac{\Delta\overline{p}}{c} + M\,\left(\,\overline{\rho}\,\Delta U + U\,\Delta\overline{\rho}\,\right)\right] \\ M\,\dfrac{\Delta\overline{p}}{\overline{\rho}}\,\mathbf{n} + |U|\,\Delta\tilde{\mathbf{u}} + \left[\,c\left(1+M^2\right) - |U|\,\right]\left(\Delta U + \dfrac{U}{\overline{\rho}}\,\Delta\overline{\rho}\right)\,\mathbf{n} \\ |U|\,\Delta\widetilde{\phi_\ell} \end{bmatrix} \tag{32}$$

where $M = (U/2)/c$ is the pseudo Mach number.

The discretization of the viscous terms is obtained by using a discrete form of the Gauss theorem leading to a central approximation of the viscous fluxes.[19]

The time integration of the set of coupled ordinary differential equations (24) is performed by a five-stage Runge-Kutta algorithm. Local time-stepping, implicit residual smoothing, and multigrid are used to accelerate the convergence to the steady-state solution. [19] In the local time-stepping procedure, the equations are advanced in time by the maximum time-step in each mesh cell. The local time-step is calculated by considering stability limitations due to both the convective and viscous eigenvalues of the system. The stability range of the time integration scheme is increased by implicitly smoothing the residuals at each stage. The right hand side residual $\mathcal{R}$ of Eqs. (24) is thus replaced by the average $\overline{\overline{\mathcal{R}}}$ of itself and the neighbouring residuals, following the expression

$$(1-\delta\,\nabla_k^2)\,(1-\delta\,\nabla_j^2)\,(1-\delta\,\nabla_i^2)\,\overline{\overline{\mathcal{R}}}=\mathcal{R} \tag{33}$$

where ∇_i^2 is the second-order central differencing in the i-direction and $\delta = 0.5$ is used in all the computations. Finally, in Eqs. (24) a multigrid algorithm is employed for pressure and momentum in order to accelerate the convergence on the fine mesh by damping out the low-frequency error components by means of iterations on coarser meshes. Coarser meshes are generated by eliminating alternate points in each coordinate direction. The restriction operator used to transfer the solution to a coarser grid is a volume-weighted average of the eight surrounding cell-centered values. Preconditioned residuals are transferred from fine to coarse meshes by injection. A forcing function is constructed so that the solution on a coarse mesh is driven by the residuals collected on the next finer mesh. The forcing function for a cell on the coarse grid is calculated by summing the residuals of its constituent fine grid cells. When the coarsest mesh is reached, the corrections are transferred to the next finer mesh by trilinear interpolation. The corrections are implicitly smoothed before updating the finer grid solution by using constant coefficients in the smoothing scheme. According to the standard W-cycle multigrid algorithm, for the coarser grid first-order upwind numerical dissipation is used [$\omega = 0$ in Eqs. (31)]. A Full Multigrid method to provide a starting solution and a multiblock partitioning of complex computational domains may be employed.

Boundary Conditions

On the inflow boundary, free-stream values of velocity and scalars are imposed while the pressure is extrapolated from the internal domain. On the outflow boundary, scalars are extrapolated, pressure is fixed, and the extrapolated value of velocity is added to a constant chosen in order to satisfy at each iteration the global conservation of mass in the computational domain. On a solid wall, zero-gradient boundary conditions are set for pressure and scalars and the no-slip condition is enforced on the velocity. A "wall function" approach[12] is used for the turbulent quantities. The "law of wall" is solved by a Newton-Raphson method in order to obtain the friction velocity u_τ. The values of k and ε in cells immediately adjacent to solid walls are obtained according to

$$k = \frac{u_\tau^2}{\sqrt{c_\mu}}\,, \qquad \varepsilon = \frac{u_\tau^3}{\chi\,\zeta} \tag{34}$$

where $\chi = 0.42$ and ζ is the distance of the cell center from wall. The value of u_τ is also used to fix the value of μ_t at the wall such that the shear stress at the wall is equal to $\rho\, u_\tau^2$.

Results

Two-dimensional Channel and Circular Duct

Solution accuracy and convergence characteristics of the code were initially tested by simulating a laminar flow in a 2-D channel and circular duct. The 2-D channel is 2 m long and 1 m high, the duct is 2 m long and the diameter is 1 m. A parabolic velocity profile with mean value $U = 0.1$ m/s is specified at entrance. A uniform velocity initial solution is fixed. Re based on 1 m is 50 and 100 for the 2-D and axisymmetric case respectively. The Mach number is $3 \cdot 10^{-3}$. Due to flow symmetry, a grid with only one cell in the azimuthal direction is used. The grid has 80×40 cells in the axial and radial direction respectively and four multigrid levels were used.

Preliminary experiments studied the influence of β on the convergence of the 2-D channel. In Fig. 1 the convergence histories for β_0 equal to 0.1, 1, 10, and 100 are shown. Here the logarithm of L_2-norm of the pressure residual is plotted versus the number of iterations (the first iteration residual is scaled to one). Fig. 1 shows that convergence is best for $\beta_0 = 10$. As noted before, when Re is low the convergence characteristics improve if β_0 is increased with respect to its optimum inviscid value $\beta_0 = 1$. Actually, as Re decreases it is necessary that the pressure wave fluctuations in the boundary layer go faster, according to a faster viscosity spreading adjustment. As demonstrated by the case $\beta_0 = 100$, if β_0 becomes too high the convergence slows down due to the increased bad-conditioning of the inviscid eigenvalues.

As representative quantity to check code accuracy we assumed the relative error of axial pressure gradient with respect to the analytical solution (Poiseuille flow). Machine zero accuracy is achieved for all the cases. The solutions on the 2-D 80×40 grid were found to be β-independent with respect to the pressure error. Starting from the 80×40 grid, in the multigrid strategy 40×20, 20×10, and 10×5 grids are generated. Calculations for 2-D channel and circular duct were performed on the four grids with $\beta_0 = 10$ and using the coarser grids for the multigrid cycles. Table 1 illustrates the results of our calculations and those of Cabuk *et al.* [20] where a preconditioning method is also employed. Table 1 shows the accuracy gain with decreasing grid size.

$90°$ Bend Flow

To test code on a real three-dimensional case, we studied a laminar flow in a $90°$ bend. This case is of particular interest because of the flow distortion and the secondary effects due to centrifugal forces.

The geometry of the $H = 0.1$ m square cross section bend is shown in Fig. 2. Here $L = 5H$ and $R = 14H$. A uniform velocity profile $U = 0.0932$ m/s is assigned at the inlet boundary. $Re = 205$ and the Mach number is $1.2 \cdot 10^{-4}$. The grid used for the calculation has 64 cells in the streamwise direction and is 16×16 in the cross sections (due to symmetry, the calculation was carried out in a single half of the cross section). Full multigrid with three levels was used and $\beta_0 = 10$.

In Figs. 3 and 4 a comparison is shown among our velocity profiles, the calculations of Krekovsky *et al.*[21], the calculations of Ghia and Sokhey[22], and the experiments of Mori *et al.*.[23] The velocity profiles are calculated in correspondence of $\theta = 90°$ where the skew flow is fully developed. In Fig. 3 the streamwise (y-direction) nondimensional velocity profile, scaled using the inlet velocity, is plotted on the symmetry z-plane. Besides our calculations and the results of Krekovsky and Ghia, the experimental data of Mori are also drawn. Comparison with the data of Mori is satisfactory. The shift of the velocity profile leads to a maximum that falls in the same position reported by experiments, even though the actual value at that point is slightly higher. Fig. 4 shows the nondimensional secondary velocity (i.e. the component along the x-direction) plotted versus z/H on the centerline of the duct section $[r = (R_1 - R)/2]$. Comparison of our results with those of Krekovsky and Ghia shows a qualitatively good agreement but our velocities values are lower at each point.

Laminar Backward Facing Step

Another test case that is studied is that of a two-dimensional laminar flow between a flat plate and a backward facing step. The problem has been experimentally investigated by Armaly *et al.*.[24] The geometry is showed in Fig. 5 where $H = Y = 0.5$ cm, $s = 4H$ and $L = 30H$. The flow reattaches at the distance x_1 downstream the step. From Armaly's experiments, when $Re < 800$ (Re being based on the hydraulic diameter $2H$) the flow is laminar and no three-dimensional effect is present. Furthermore, an additional recirculation-flow region appears on the upper flat plate when $Re > 400$. This zone extends downstream of the step between x_2 and x_3.

In our calculations a parabolic velocity profile with mean value $U = 1$ m/s is specified at the entrance (the corresponding Mach number is $3 \cdot 10^{-3}$). A two-blocks mesh simulates also the inlet channel. The meshes for block 1 and block 2 have 16×32 and 120×64 cells respectively and three levels of multigrid are employed. Calculations were performed at Re equal to 100, 152, 303, 389, 452, 500, 600, 700, and 800. The values of β_0 ranged from $\beta_0 = 0.01$ at $Re = 800$ to $\beta_0 = 10$ at $Re = 100$. No convergence was achieved at higher Re if $\beta_0 > 0.01$, showing that the presence of large recirculation zones require the propagation speed of pressure waves to be slow. The reattachment distances x_1/H and x_3/H and the separation distance x_2/H calculated for different Re are shown in Fig. 6, where the experiments of Armaly and the numerical results of Cabuk *et al.*,[20] Kim and Moin,[25] Rogers and Kwak[26] are also reported. There is good agreement between our results and those of the other authors.

Turbulent Backward Facing Step

The geometry of this 2-D planar turbulent test case is that of Fig. 5 where $H = 1.27$ cm, $Y = 8H$, $s = 4H$, and $L = 30H$. In the experiments performed by

Driver and Seegmiller,[27] mean velocity and turbulent kinetic energy transversal profiles have been measured at different axial positions. The profiles at $4H$ upstream the step have been used as inlet profiles in our computation. The inlet values of ε were calculated through the relation

$$\varepsilon = \frac{k^{3/2}}{0.3 \cdot Y} \,. \tag{35}$$

The Re based on the inlet mean velocity $U = 44.2$ m/s is $3 \cdot 10^5$ and the flow is fully turbulent. The value $\beta_0 = 1$ was used. The blocks 1 and 2 have 16×64 and 96×72 cells respectively.

The standard $k - \epsilon$ model predicts a reattachment length $x_1/H \simeq 5.1$, while in the experiments $x_1/H \simeq 6.2$. Therefore, the standard $k-\epsilon$ model underpredicts the experimental reattachment length. Figures 7 and 8 show the transversal profiles of the axial velocity and turbulent kinetic energy at different axial positions x/H. In all cases agreement between predicted and experimental profiles is good.

Coaxial Jet Flame with Flameholder

This test case is based on an experimental axisymmetric configuration tested by Correa and Gulati.[28] The three-block computational domain and the streamline pattern are shown in Fig. 9. The combustor is a 15×15 cm square section wind tunnel (simulated as axisymmetric), with a 3.18 mm diameter cylindrical fuel nozzle located along the axis. A 38.1 mm diameter axisymmetric bluff-body flameholder surrounds the fuel nozzle in order to create a recirculation zone. The fuel molar fraction composition is: 27.5 % CO, 32.3 % H_2, 40.2 % N_2. The fuel and air velocities are 80 m/s and 6.5 m/s, respectively. Pressure is 101000 Pa and fuel and air temperatures are 300 K. Uniform inlet velocity profiles were used for both fuel and air. The inlet values of k was $0.005 \cdot U^2$, and ε was given by Eq. (35). An axisymmetric grid with 5504 cells and a spread angle of 10° was used. Density relaxation was necessary to achieve the steady solution because of the strong density variation ($\rho_{\widetilde{f}=0}/\rho_{\widetilde{f}=1} = 7$ when $\widetilde{f''^2} = 0$), especially during the first iterations. The employed relaxation factor was 0.001.

The radial profiles of mixture fraction $\widetilde{f}$ and of its normalized variance $\sqrt{\widetilde{f''^2}}/\widetilde{f}$ at the axial station $x/d = 10$ (where d is the diameter of the fuel jet) are shown in Fig. 10-11. Here also the experiments of Correa are reported. In Fig. 12 the radial profile of $\widetilde{f}$ at $x/d = 20$ is shown. Comparison between predictions and experiments is satisfactory.

Conclusions

A numerical code for low-speed turbulent flows has been presented. A novel preconditioning method is applied to the density-based formulation suitable for both non-reacting flows and non-premixed combustion flows. The preconditioning allows to retain all the numerical characteristics of density-based codes and to overcome their difficulties when simulating low-speed flows. This solver extends explicit CFD solutions to non-reactive and reactive flows with very low Mach numbers, down to $\mathcal{O}(10^{-3})$. A MUSCL spatial discretization has been developed for the preconditioned system. This method has been used to successfully simulate laminar and turbulent cold flows as well as a combustion flow characterised by large density fluctuations. The numerical results are in agreement with experiments and with results obtained by other authors.

Acknowledgements

This work has been financially supported by the Sardinian Regional Authorities and by EC under the ESPRIT-HPCN Project 8835.

References

[1] Libby, P.A., and Williams, F.A., "Fundamental Aspects", *Turbulent Reacting Flows*, edited by P.A Libby and F.A. Williams, Topics in Applied Physics, Vol. 44, Springer-Verlag, New York, 1980, pp. 1-43.

[2] Chorin, A.J., "Numerical Solution of Navier-Stokes Equations", *Mathematics of Computation*, Vol. 22, 1968, pp. 745-762.

[3] Patankar, S.V., *Numerical Heat Transfer and Fluid Flow*, Hemisphere Publishing Co., New York, 1980.

[4] Chorin, A.J., "A Numerical Method for Solving Incompressible Viscous Flow Problems", *Journal of Computational Physics*, Vol. 2, 1967, pp. 12-26.

[5] Merkle, C.L., and Choi, Y.-H., "Computation of Low-Speed Compressible Flows with Time-Marching Procedures", *International Journal for Numerical Methods in Engineering*, Vol. 25, 1988, pp. 293-311.

[6] Turkel, E., "Preconditioning Methods for Solving the Incompressible and Low Speed Compressible Equations", *Journal of Computational Physics*, Vol. 72, 1987, pp. 277-298.

[7] Rogers, S.E., and Kwack, D., "Steady and Unsteady Solutions of the Incompressible Navier-Stokes Equations", *AIAA Journal*, Vol. 29, 1991, pp. 603-610.

[8] van Leer, B., Lee, W.T., and Roe, P.L., "Characteristic Time Stepping or Local Preconditioning of the Euler Equations", AIAA Paper 91-1552, 1991.

[9] Choi, Y.-H., and Merkle, C.L., "The Application of preconditioning in Viscous Flows", *Journal of Computational Physics*, Vol. 105, 1993, pp. 207-223.

[10] Shuen, J.-S., Chen, K.-H., and Choi, Y., "A Coupled Implicit Method for Chemical Non-equilibrium Flows at All Speeds", *Journal of Computational Physics*, Vol. 106, 1993, pp. 306-318.

[11] Dailey, L., and Pletcher, R., "Evaluation of Multigrid Acceleration for Precondiotioned Time-Accurate Navier-Stokes Algorithms", AIAA Paper 95-1668, 1995.

[12] Launder, B.E., and Spalding, D.B., "The Numerical Computation of Turbulent Flows", *Computer Methods in Applied Mechanics and Engineering*, Vol. 3, 1974, pp. 269-289.

[13] Bilger, R,W., "Turbulent Flows with Nonpremixed Reactans", *Turbulent Reacting Flows*, edited by P.A Libby and F.A. Williams, Topics in Applied Physics, Vol. 44, Springer-Verlag, New York, 1980, pp. 65-113.

[14] Gordon, S., and McBride, B., "Computer Program for Calculation of Complex Chemical Equilibrium Compositions", NASA SP-273, 1971.

[15] Girimaji, S.S., "Assumed β-pdf Model for Turbulent Mixing Validation and Extension to Multiple Scalar Mixing", *Combustion Sciences and Technology*, Vol. 78, 1991, pp. 177-196.

[16] Abramowitz, M., and Stegun, I.A., *Handbook of Mathematical Functions*, National Bureau of Standards, Washington, 1964.

[17] Roe, P.L., "Approximate Riemann Solver, Parameter Vectors, and Difference Schemes", *Journal of Computational Physics*, Vol. 43, 1981, pp. 357-372.

[18] van Leer, B., "Towards the Ultimate Conservative Difference Scheme V, A Second-Order Sequel to Godunov's Methos", *Journal of Computational Physics*, Vol. 32, 1979, pp. 101-136.

[19] Martinelli, L., "Calculations of Viscous Flows with a Multigrid Method", Ph.D. Thesis, MAE Department, Princeton Univ., Princeton, NJ, Oct. 1987.

[20] Cabuk, H., Sung, C.-H., and Modi, V., "Explicit Runge-Kutta Method for Three-Dimensional Internal Incompressible Flows", *AIAA Journal*, Vol. 30, 1992, pp. 2024-2031.

[21] Krekovsky, J., Briley, W., and McDonald, H., "Prediction of Laminar and Turbulent Flows in Strongly Curved Ducts", NASA CR-3388, 1981.

[22] Ghia, K., and Sokhey, J., "Laminar Incompressible Viscous Flows in Curved Ducts of Rectangular Cross Sections", *ASME Journal of Fluid Engineering*, Vol. 4, 1977, pp. 640-648.

[23] Mori, V., Uchida, Y., and Uken, T., "Forced Convective Heat Transfer in a Curved Channel with a Square Cross Section", *International Journal of Heat Transfer*, Vol. 14, 1971, pp. 1787-1805.

[24] Armaly, B., Durst, F., Pereira, J., and Schonung, B., "Experimental and Theoretical Investigation of Backward-Facing Step Flow", *Journal of Fluid Mechanics*, Vol. 127, 1983, pp. 473-496.

[25] Kim, J., and Moin, P., "Application of a Frctional-Step Method to Incompressible Navier-Stokes Equations", *Journal of Computational Physics*, Vol. 59, 1985, pp. 308-323.

[26] Rogers, S. E., and Kwak, D., "An Upwind Differencing Scheme for the Time-Accurate Incompressible Navier-Stokes Equations", AIAA Paper 88-2583, 1988.

[27] Driver, D.M., and Seegmiller, H.L., "Features of a Reattaching Turbulent Shear Layer in Divergent Channel Flow", *AIAA Journal*, Vol. 23, 1985, pp. 163-171.

[28] Correa, S.M., and Gulati, A., "Measurements and Modeling of a Bluff Body Stabilized Fame", *Combustion and Flame*, Vol. 89, 1992, pp. 195-213.

Table 1 2D channel and circular duct. Pressure gradient relative errors respect to analytic solution for $\beta_0 = 10$: $\square$, present calculations; $\triangle$, Cabuk *et al.*.[20]

Grids	2D channel		Circular duct	
	$\square$	$\triangle$	$\square$	$\triangle$
10×5	2.8%	5.1%	0.4%	15.7%
20×10	0.6%	0.9%	0.27%	3.1%
40×20	0.16%	0.15%	0.252%	0.4%
80×40	0.04%	0.02%	0.250%	-

Captions of Figures

Fig. 1 2-D channel, 80×40 grid. Pressure residual *vs* number of iterations: $\square$, $\beta_0 = 0.1$; $\triangle$, $\beta_0 = 1$; $\diamondsuit$, $\beta_0 = 10$; $\bigcirc$, $\beta_0 = 100$.

Fig. 2 Geometry of bend flow.

Fig. 3 Bend flow. Non-dimensional streamwise velocity profile at $z = H/2$ and $\theta = 90°$: ——, present calculation; $\square$, Krekovsky *et al.*;[21] $\triangle$, Ghia and Sokhey;[22] $\diamondsuit$, Mori *et al.*.[23]

Fig. 4 Bend flow. Non-dimensional secondary velocity profile at $r = (R_1 - R)/2$ and $\theta = 90°$: ——, present calculation; $\square$, Krekovsky *et al.*;[21] $\triangle$, Ghia and Sokhey.[22]

Fig. 5 Geometry of backward facing step.

Fig. 6 Laminar backward facing step. Separation (x_1, x_2) and reattachment (x_3) points at different Re: —×—, present calculations; $\square$, Armaly *et al.*;[24] $\triangle$, Kim and Moin;[25] $\diamondsuit$, Cabuk *et al.*;[20] $\bigcirc$, Rogers and Kwak.[26]

Fig. 7 Turbulent backward facing step. Velocity profiles at different distances x/H from the step: ——, present calculation; $\bigcirc$, Driver and Seegmiller.[27]

Fig. 8 Turbulent backward facing step. Turbulent kinetic energy at different distances x/H from the step: ——, present calculation; $\bigcirc$, Driver and Seegmiller.[27]

Fig. 9 Geometry and streamlines of coaxial jet flame.

Fig. 10 Coaxial jet flame. Mixture fraction $\tilde{f}$ radial profile at distance $x/d = 10$ from the bluff-body: ——, present calculation; $\bigcirc$, Correa and Gulati.[28]

Fig. 11 Coaxial jet flame. Normalized mixture fraction variance $\sqrt{\widetilde{f''^2}}/\widetilde{f}$ at distance $x/d = 10$ from the bluff-body: —, present calculation; ○, Correa and Gulati.[28]

Fig. 12 Coaxial jet flame. Mixture fraction $\widetilde{f}$ radial profile at distance $x/d = 20$ from the bluff-body: —, present calculation; ○, Correa and Gulati.[28]

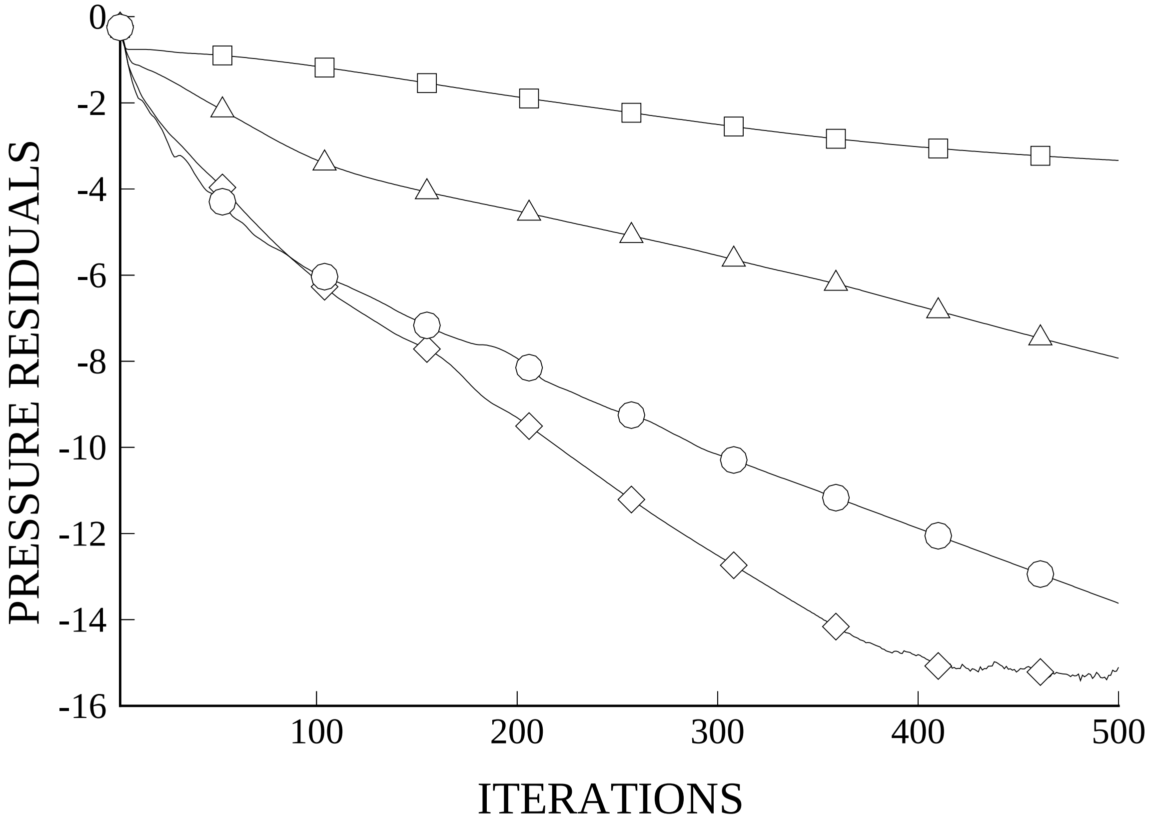
0
-2
-4
-6
-8
-10
-12
-14
-16
100
200
300
400
500
PRESSURE RESIDUALS
ITERATIONS

Figure 1:

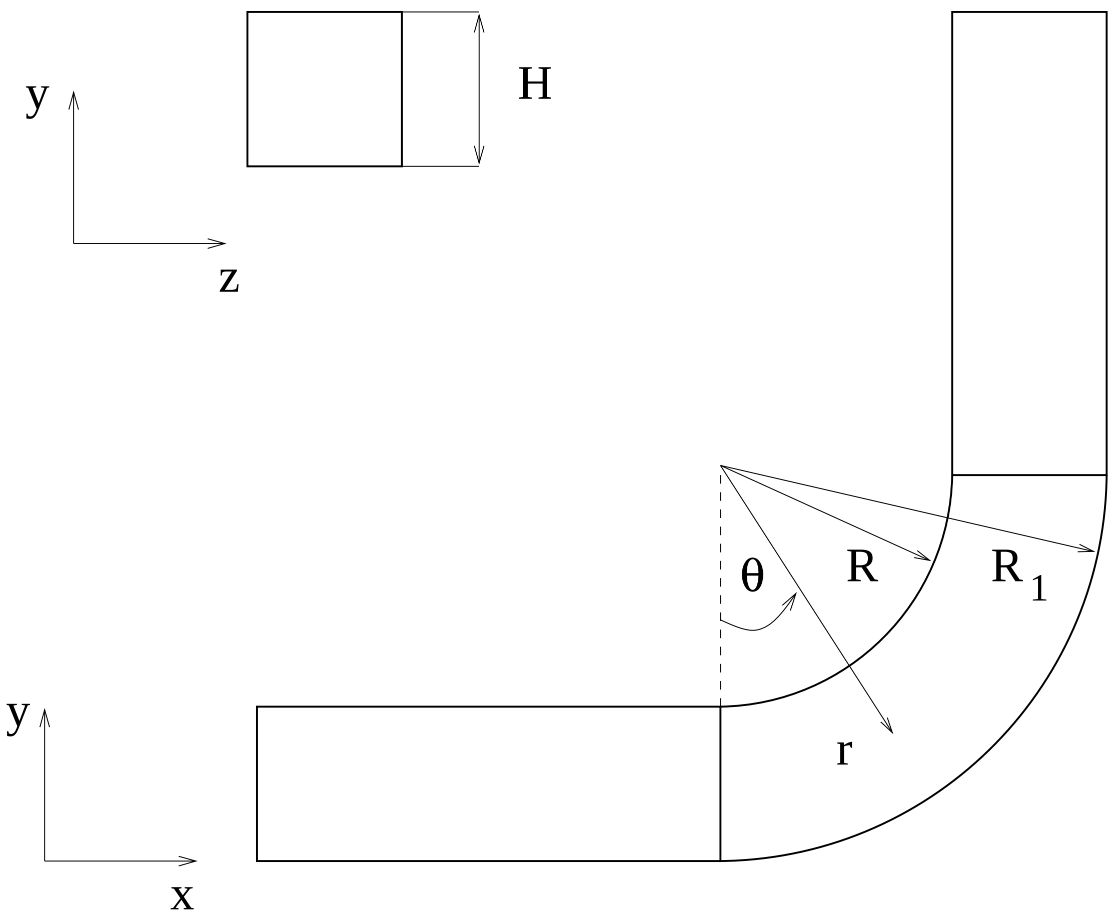

Figure 2:

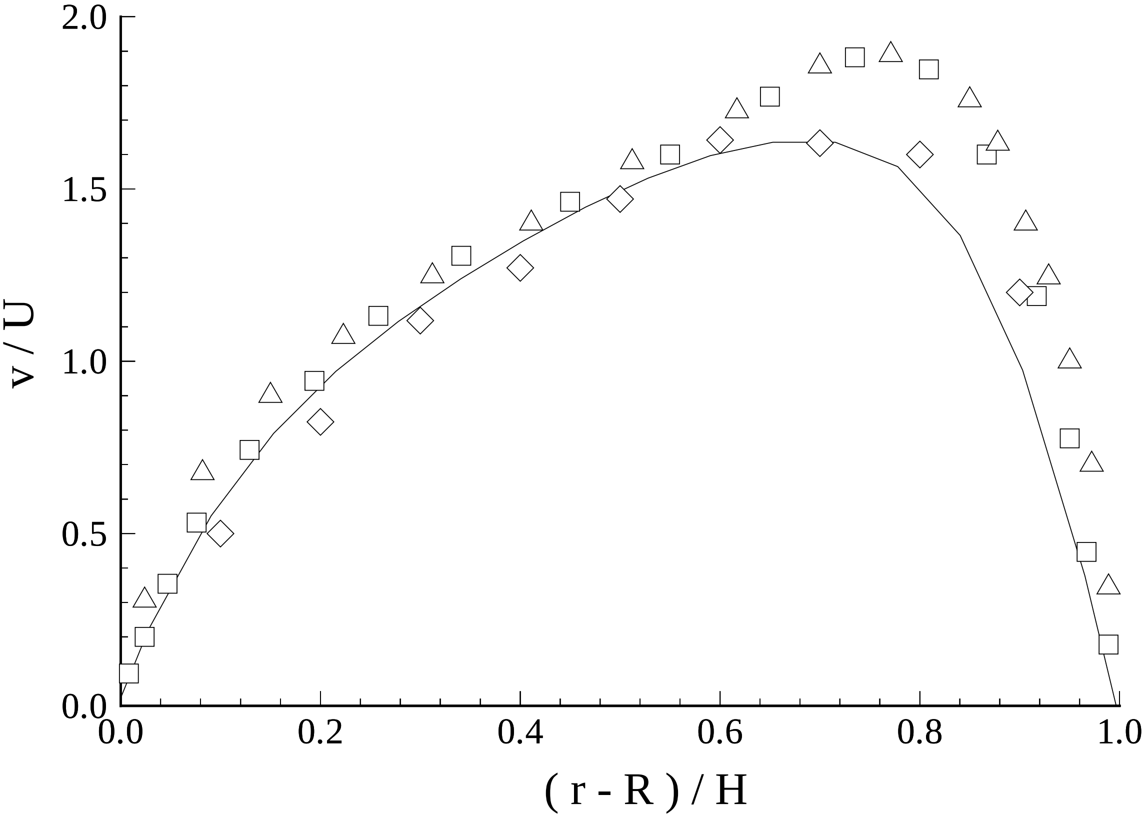

Figure 3:

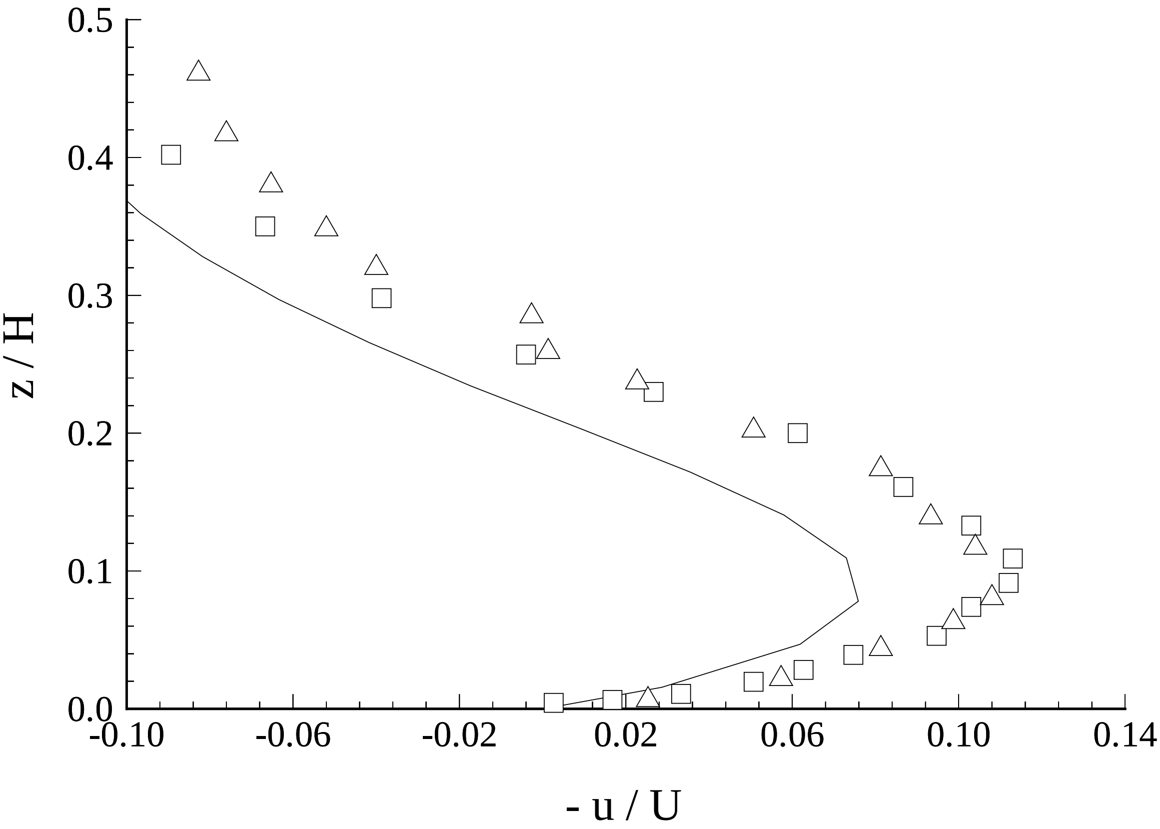

Figure 4:

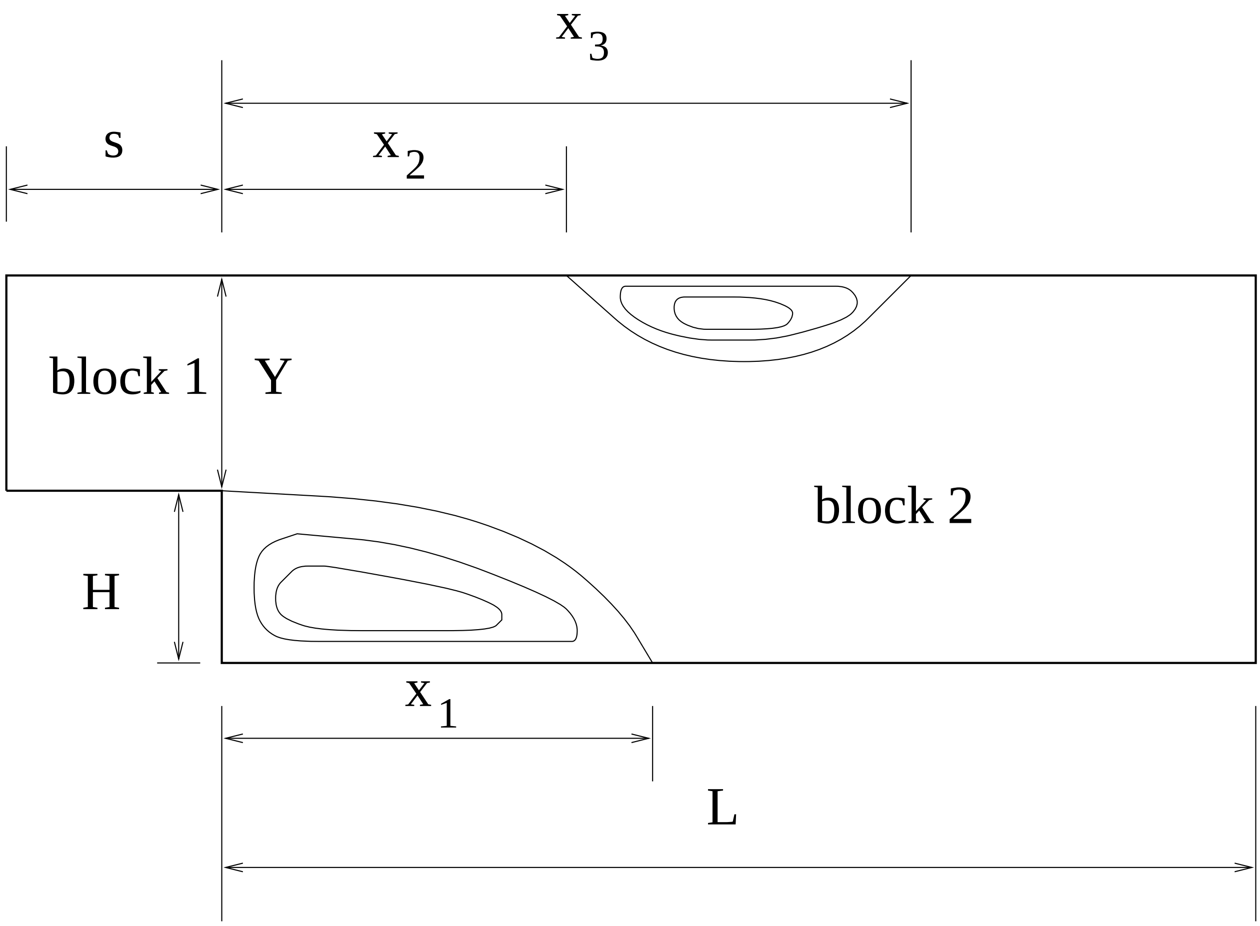

Figure 5:

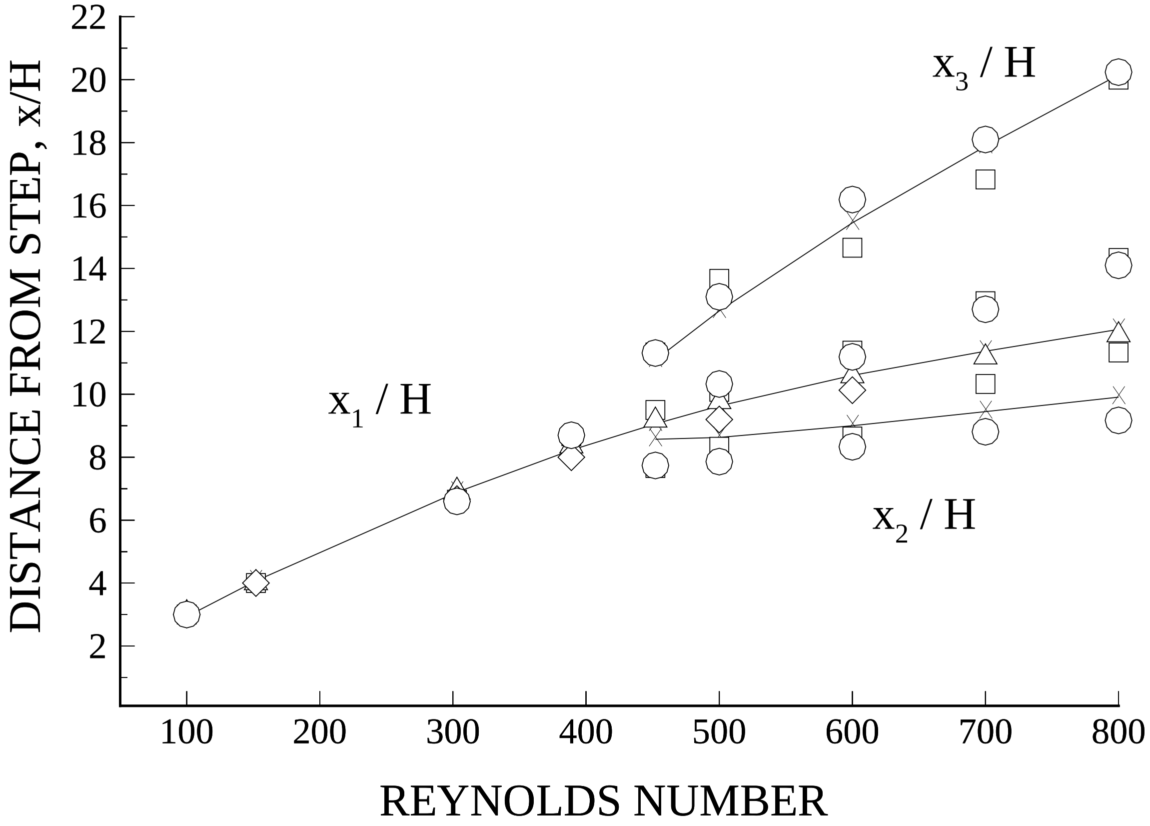
DISTANCE FROM STEP, x/H
REYNOLDS NUMBER
x3 / H
x1 / H
x2 / H
22
20
18
16
14
12
10
8
6
4
2
100
200
300
400
500
600
700
800

Figure 6:

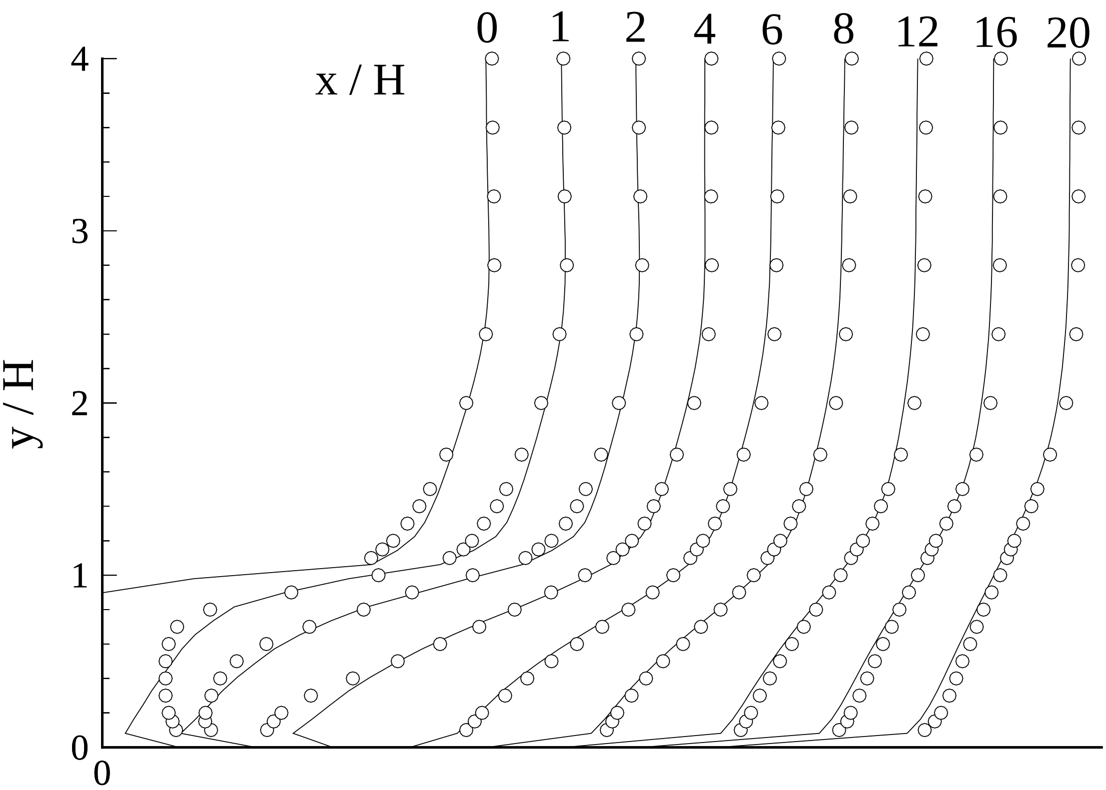

Figure 7:

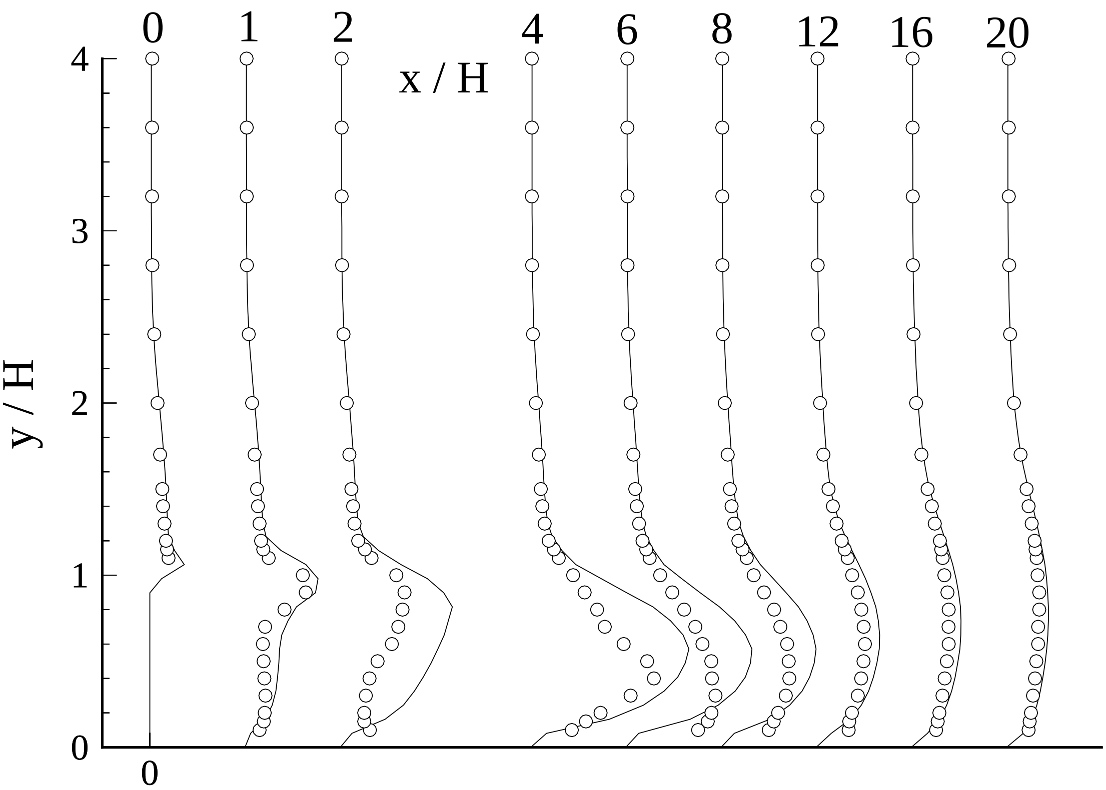

Figure 8:

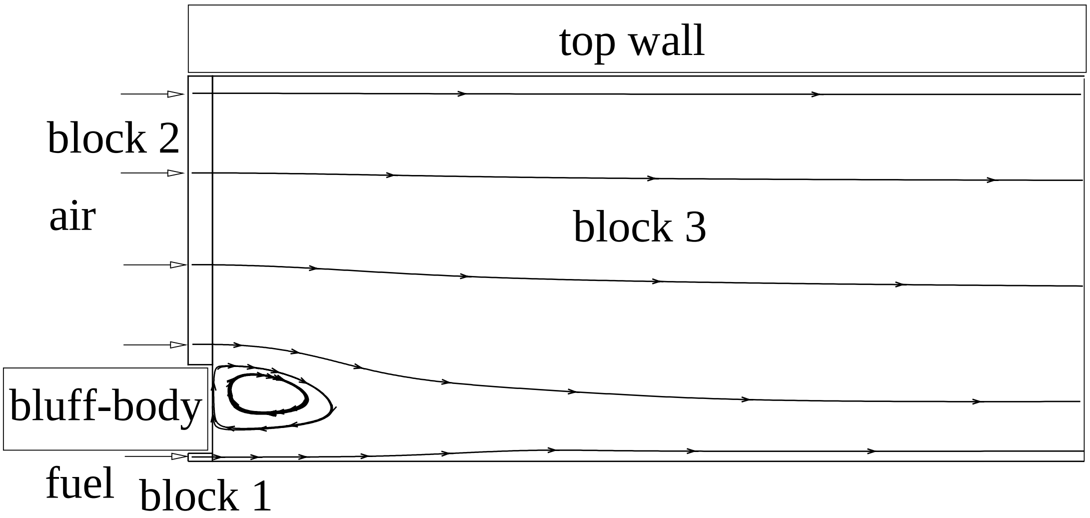

Figure 9:

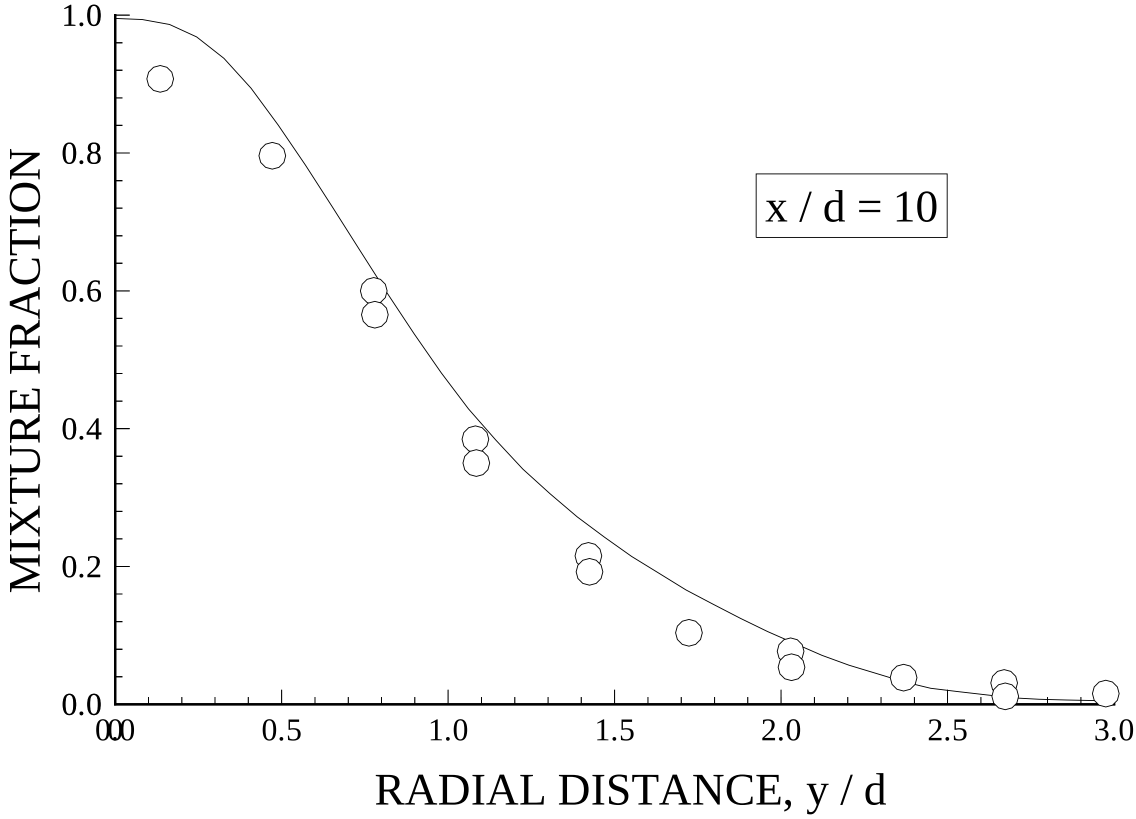
MIXTURE FRACTION
1.0
0.8
0.6
0.4
0.2
0.0
x / d = 10
0.0
0.5
1.0
1.5
2.0
2.5
3.0
RADIAL DISTANCE, y / d

Figure 10:

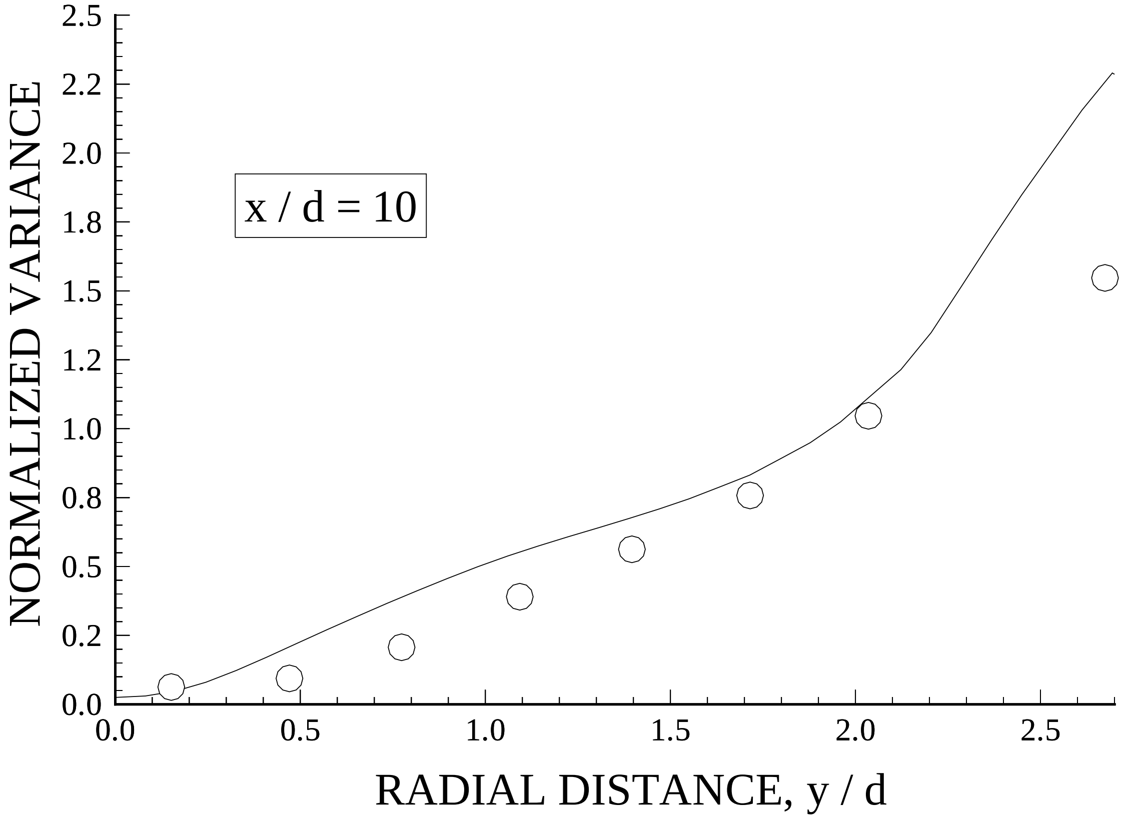

x / d = 10
NORMALIZED VARIANCE
RADIAL DISTANCE, y / d
0.0
0.2
0.5
0.8
1.0
1.2
1.5
1.8
2.0
2.2
2.5
0.0
0.5
1.0
1.5
2.0
2.5

Figure 11:

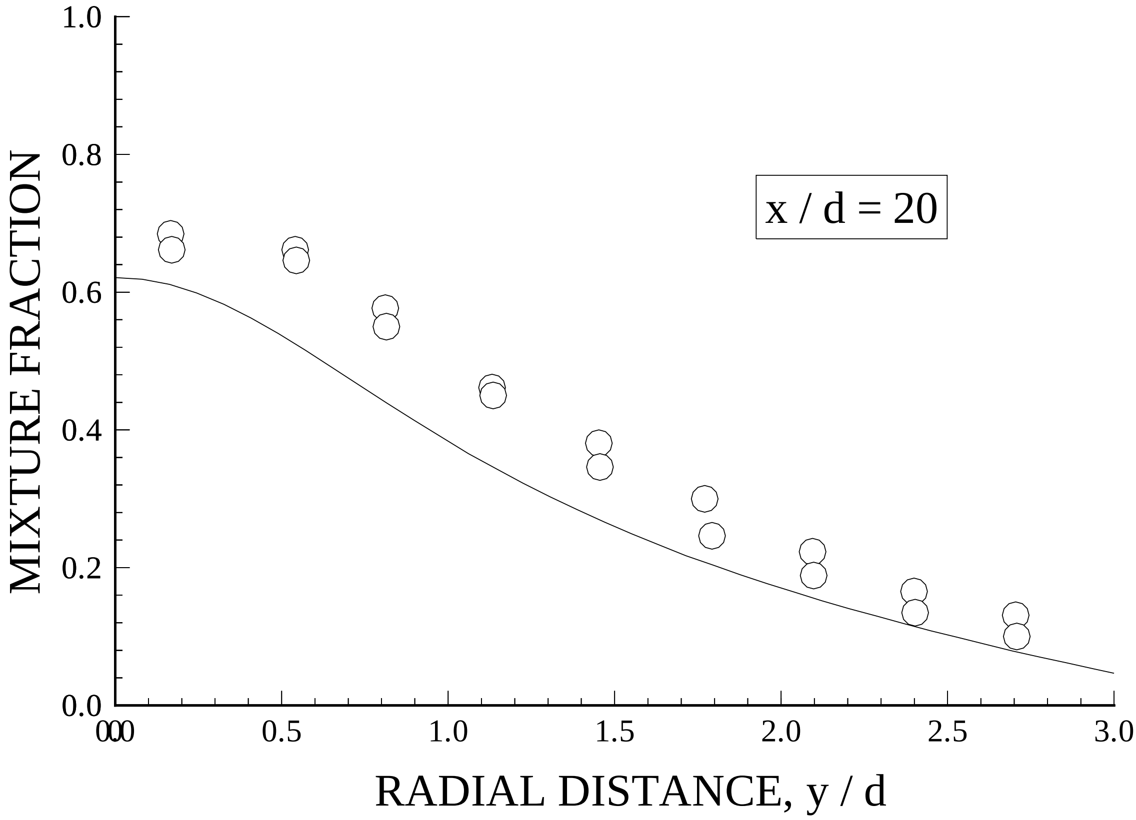

1.0
0.8
0.6
0.4
0.2
0.0
MIXTURE FRACTION
x / d = 20
0.0
0.5
1.0
1.5
2.0
2.5
3.0
RADIAL DISTANCE, y / d

Figure 12: